Lissajous-trajectory scanning optical coherence photoacoustic microscopy for zebrafish larva imaging

Original

Lissajous-trajectory scanning optical coherence photoacoustic microscopy for zebrafish larva imaging / Bugyi, L., Schmitner, N., Kimmel Robin, A., Meyer, D., Zhou, Q., Haindl, R., Salvi, M., Rotunno, G., Meiburger Kristen, M., Distel, M., Sturtzel, C., Yuan, Y.i., Drexler, W., Liu, M.. - In: JPHYS PHOTONICS. - ISSN 2515-7647. - 8:1(2026). [10.1088/2515-7647/ae392c]

Publisher:
IOP

Published
DOI:10.1088/2515-7647/ae392c

JPhys Photonics

Lissajous-trajectory scanning optical coherence photoacoustic microscopy for zebrafish larva imaging

To cite this article: Lukasz Bugyi *et al* 2026 *J. Phys. Photonics* **8** 015042

IOP Publishing J. Phys. Photonics 8 (2026) 015042 https://doi.org/10.1088/2515-7647/ae392c

Journal of Physics: Photonics

OPEN ACCESS

RECEIVED
6 September 2025

REVISED
25 November 2025

ACCEPTED FOR PUBLICATION
15 January 2026

PUBLISHED
30 January 2026

PAPER

Lissajous-trajectory scanning optical coherence photoacoustic microscopy for zebrafish larva imaging

Lukasz Bugyi[1], **Nicole Schmitner**[2], **Robin A Kimmel**[2], **Dirk Meyer**[2], **Qifa Zhou**[3], **Richard Haindl**[1], **Massimo Salvi**[4], **Giulia Rotunno**[4], **Kristen M Meiburger**[4], **Martin Distel**[5], **Caterina Sturtzel**[6], **Yi Yuan**[7,*], **Wolfgang Drexler**[1] and **Mengyang Liu**[1,*]

[1] Center for Medical Physics and Biomedical Engineering, Medical University of Vienna, Währinger Gürtel 18-20, AKH 4L, 1090 Vienna, Austria
[2] Institute of Molecular Biology, Leopold-Franzens-University Innsbruck, Technikerstraße 25, 6020 Innsbruck, Austria
[3] USC Roski Eye Institute, University of Southern California, 1450 San Pablo Street, 4th Floor, Los Angeles, CA 90033, United States of America
[4] Polito^{BIO}Med Lab, Biolab, Department of Electronics and Telecommunications, Politecnico di Torino, Corso Duca degli Abruzzi 24, 10129 Torino, Italy
[5] Huntsman Cancer Institute, University of Utah, 2000 Circle of Hope, Salt Lake City, UT 84112, United States of America
[6] St. Anna Kinderkrebsforschung, Zimmermannplatz 10, 1090 Vienna, Austria
[7] School of Electrical Engineering and the Key Laboratory of Intelligent Rehabilitation and Neuromodulation of Hebei Province, Yanshan University, Qinhuangdao, People's Republic of China
[*] Authors to whom any correspondence should be addressed.

E-mail: yuanyi513@ysu.edu.cn and mengyang.liu@meduniwien.ac.at

Keywords: photoacoustic microscopy, optical coherence tomography, Lissajous, zebrafish, multimodal imaging

Supplementary material for this article is available online

Abstract

As an important vertebrate animal model for development and human disease, research on zebrafish has been using many different imaging methods. Among them, optical coherence microscopy and photoacoustic microscopy (PAM) are gradually gaining popularity due to their complementary contrast mechanisms and non-invasive nature. This work demonstrates a combined optical coherence PAM system using Lissajous scanning trajectories for zebrafish imaging. The system configuration enables a large field of view (up to 11.8 mm × 25.2 mm) with uniform high resolution (1.8 μm lateral) and uniform sensitivity across the entire scanning area. The voice-coil-enabled Lissajous trajectories yield high scanning speed, while maintaining precise coregistration between modalities. A specially designed deep learning-based upsampling model has been trained to leverage unique characteristics of the Lissajous scanning pattern, reducing acquisition time by up to 70% while preserving image quality. The system's capabilities are demonstrated through high-resolution imaging of zebrafish larvae, revealing detailed vascular networks and tissue structures. This novel approach provides a powerful tool for non-invasive, multimodal imaging of zebrafish development and disease models beyond typical size boundaries.

1. Introduction

With their advantages in large-scale genetic mutant and therapeutic compound screenings, zebrafish have become a powerful disease model in biomedical research [1]. Numerous studies have demonstrated the unique advantages of using zebrafish across diverse fields of research [2–6]. On top of its genetic similarity to human and other biological advantages compared with mouse models, zebrafish's increasing popularity can be attributed to its small size and optical transparency [1], which easily permits dynamic processes to be monitored *in vivo* with optical imaging methods. Among all the optical imaging methods used in zebrafish studies, fluorescence imaging techniques such as confocal microscopy, multiphoton microscopy, and light sheet microscopy are the typical choice due to their wide availability [7–10]. However, these fluorescence imaging techniques need fluorescent labels, posing a major limitation to its use in functional *in vivo* imaging [7]. As an alternative, nonlinear optical imaging methods [11–13] were shown as label-free imaging approaches to study zebrafish. However, these nonlinear imaging methods all suffer from very shallow imaging depth, hindering their use in zebrafish imaging.

In light of the imaging challenges in zebrafish research, optical coherence tomography (OCT) and photoacoustic imaging have been suggested as suitable tools for non-invasive imaging approaches for zebrafish. As of now, numerous works have been done to establish *in vivo* OCT imaging protocol for the zebrafish eye with various applications [14–19]. In addition, different OCT configurations have also been applied for other types of studies using zebrafish [20–25]. Photoacoustic imaging, which uses optical absorption as the contrast mechanism, has also shown significant value in zebrafish imaging. Using photoacoustic tomography (PAT), whole-body adult zebrafish can be imaged non-invasively allowing visualization of all major organs [26–30]. When higher resolution is needed, photoacoustic microscopy (PAM) is the better option for zebrafish imaging, especially for embryos and larvae [31–35]. A unique advantage of PAM in zebrafish imaging is its compatibility with a variety of contrast agents for molecular imaging [36–38].

Given the complementary contrast mechanisms of OCT and PAM, using dual modal optical coherence PAM (OC-PAM) for zebrafish imaging can meet the requirements of many zebrafish-based studies. Employing a fiber optic sensor, OC-PAM imaging of zebrafish was accomplished in a transmission mode system [36]. Reflection mode OC-PAM for zebrafish imaging was demonstrated using an akinetic sensor, which permitted relatively large field of view (FOV) [37]. This reflection mode OC-PAM system was later upgraded with functional extensions, which enabled the study of zebrafish pulsation, blood oxygen saturation, and vessel blood flow velocity [38]. However, the optical detection methods used in the above-mentioned OC-PAM systems such as the fiber optic sensor [39] and the akinetic sensor [40] both suffer from low sensitivity and are limited in bandwidth, hence yielding non-optimal axial resolution photoacoustically. The FOV of the systems is also limited with decreasing sensitivity when the laser-scanned beam leaves the central region.

Beyond its application in zebrafish imaging, many other OC-PAM configurations have been implemented with various features [41, 42]. When reflection mode is needed, the most commonly seen realization of OC-PAM is to use an obliquely positioned piezoelectric transducer while the excitation beam of PAM and the sample beam of OCT being scanned over the sample [43–50]. Although the speed can be as fast as the laser repetition rate using this straightforward configuration, the use of unfocused ultrasound transducer and the angled positioning of it limits the sensitivity and FOV of such systems. In order to overcome this downside, those systems typically utilize high averaging, offsetting their short frame time. One compromise between speed and sensitivity is to use a cylindrically focused transducer and scan the laser beams in just one direction by a galvanometer mirror [51]. Such an implementation has been shown to have high spatial and temporal resolution, but only in one direction. Other efforts of using optical detection methods for OC-PAM have been proposed [52, 53], but they are either slow or suffer from non-uniform sensitivity and limited FOV.

It is known that mechanical scanning with confocal and coaxial alignment of light and sound is the only method to guarantee the highest sensitivity, large FOV, and consistent performance [54], however, mechanical scanning has not seen much improvement since the voice-coil-based raster scanning PAM systems were demonstrated [55, 56]. In this work, we designed an OC-PAM system which has these features together with a relatively short imaging time. The novelty of this new OC-PAM system lies in the use of Lissajous scanning trajectories and AI-based upsampling algorithms. While we demonstrate the system using a focused ring transducer, the scanning and image reconstruction protocol are directly and broadly translatable to other detection methods.

2. Materials and methods

2.1. Lissajous trajectory

A 2D Lissajous trajectory can be achieved by sinusoidal movement in two orthogonal directions [57]. It can be mathematically expressed as

$$x(t) = X_0 + \frac{A}{2}\cos(2\pi f_x t)$$

$$y(t) = Y_0 + \frac{B}{2}\cos(2\pi f_y t)$$

where (X_0, Y_0) are the starting points of the scan; A and $\boldsymbol{B}$ are the travel range in the x and y directions, respectively; f_x and f_y are the scan frequency in the two axes, respectively. The pattern repeats itself with

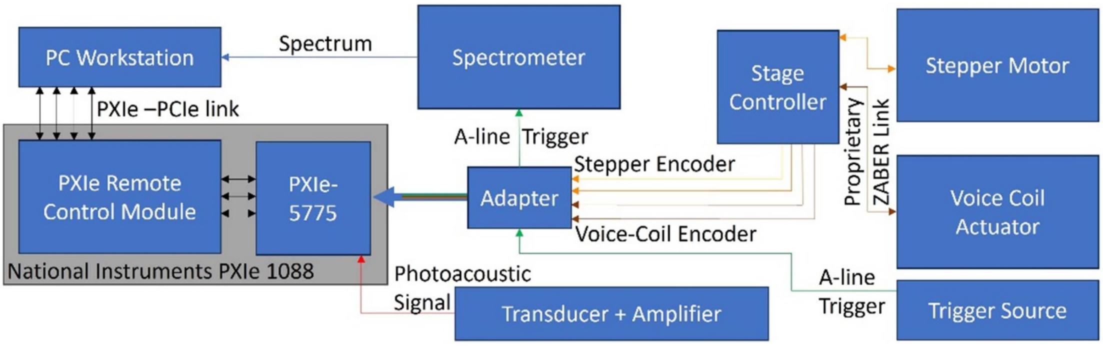

Figure 1. Schematic of electrical connections for position tracking of the OC-PAM system. PXIe-5775 (FPGA) is connected to the PXIe remote control module through backplate connections within the PXIe 1088 chassis. The adapter is a signal conditioning circuit allowing different electrical signals to be connected to the FPGA. Please note that while the A-line trigger signal enters and exits through the adapter, this is not a passthrough, the signal is processed onboard the FPGA.

a period of T determined by

$$T = \mathrm{lcm}\left(\frac{1}{f_x}, \frac{1}{f_y}\right).$$

When f_x and f_y are integers, T takes the form of $T = \frac{1}{k}$, where $k = 1, 2, 3\ldots$ This means that the pattern closes at most within 1 s, which may not be sufficient to create a dense enough pattern using physically realizable movement frequencies and laser repetition rates. But when f_x and f_y are non-integers, T is determined by

$$T = \mathrm{lcm}\left(\frac{1}{f_x}, \frac{1}{f_y}\right) = \mathrm{lcm}\left(\frac{a}{b}, \frac{c}{d}\right) = \frac{\mathrm{lcm}\,(a, c)}{\mathrm{gcd}\,(b, d)} \qquad a, b, c, d \in \mathbb{N}$$

which allows for T above 1 s and creation of patterns which are physically realizable. These patterns can then provide high densities suitable for microscopy applications. The relation between pattern density and frequency pair is highly-nonlinear and lacks an analytical model. The presence of the $\mathrm{gcd}\,(b, d)$ function in the denominator of the closing-time expression suggests that selecting b and d to be co-prime should prevent it from closing too early to form a dense pattern. This principle provides the starting point for experimental testing of the filling ratio (FR) for any given frequency pair. Here, FR is defined as the ratio of the number of pixels in a reconstructed image, where at least one A-line has been recorded, to the total number of pixels in the reconstructed image. We deem FR above 85% to be satisfactory, as it falls in line with FR typically accepted for microscopy applications [58, 59]. In our setup, the Lissajous trajectory is enabled by a voice coil linear actuator (DMQ12L-AE55T10A, Zaber Technologies Inc., Canada) as the fast axis and a stepper motor linear stage (LSM025A-E03T4A, Zaber Technologies Inc., Canada) as the slow axis. The travel range of the voice coil actuator is 12 mm with a repeatability of <0.5 μm. Its maximum acceleration reaches 245 $\mathrm{m\,s^{-2}}$ and has an encoder count size of 1 nm. The stepper motor stage has a longer travel range of 25.4 mm and a repeatability of <3 μm. The rotary quadrature encoder for the 2-phase stepper motor has a resolution of 800 states per revolution providing a resolution of 762 nm. These features enable a large FOV with a maximum dimension of 12 mm × 25.4 mm. The communication between the voice coil actuation, the stepper motor, and the workstation is achieved using a controller (X-MCC2-ENG3975, Zaber Technologies Inc., Canada) on the stage side and an FPGA (PXIe-5775, National Instruments, USA) on the workstation side. More specifically, the controller transmits the differential encoder signals over dedicated single-line cables connected to the binary inputs of the FPGA, which is controlled using a PXI remote control module (PXIe-8398, National Instruments, USA). Whereas the workstation receives input from the stages via a PXI controller (PCIe-8398, National Instruments, USA), it can also send commands to the controllers directly via serial communication. The detailed signal schematic of the system is illustrated in figure 1.

Setting $f_x = 27.0271$ Hz, $f_y = 0.99425$ Hz, $A = 12$ mm, $B = 25.4$ mm, and the laser repetition rate = 100 kHz, which represent the theoretical maximum values of the components selected when no payload is present, the Lissajous trajectory over selected time points are shown in figure 2. Because after 100 s the trajectory lines are too dense to distinguish, we use color coding to represent the density of points. Each pixel corresponds to a dimension of 40 μm × 40 μm and the color represents the number

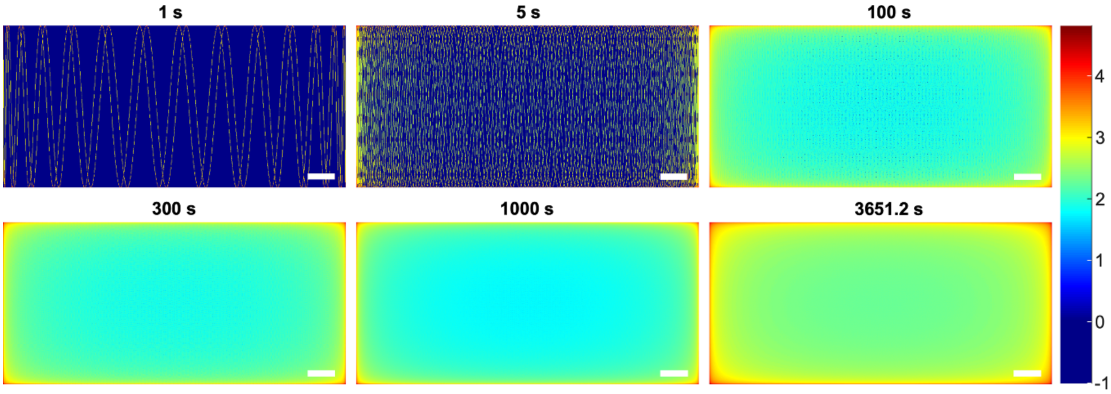

Figure 2. Simulated scanning density map of 12 mm × 25.4 mm FOV scanned using a Lissajous pattern after given number of seconds. Pixel colors correspond to $\log_{10}$ of the number of points which fall into the area represented by that pixel. Scalebar = 2 mm, pixel size = 40 μm × 40 μm.

of times the Lissajous trajectory traverses this pixel by this time point. At 3651.2 s, the FR reaches 99% coverage assuming a lateral spot size of 2 μm, and we choose this time as the end time of simulation.

In our actual experiments, due to the payload on the voice coil actuator, we used $f_x = 11.09$ Hz, $f_y = 0.569$ Hz, with amplitudes being adjusted to fit the imaged sample. Owing to constant imaging performance of the system across the FOV, we could locate the imaging object in a quick, sparser pattern scan, and after selecting it, automatically adjust dense pattern scan parameters to tightly fit the object.

2.2. OC-PAM system

The OC-PAM system consists of a spectral domain OCT subsystem using a compact polarization-aligned 840 nm broadband source (EBD290002, EXALOS, Switzerland), whose 160 nm bandwidth and constant polarization state across the full spectral output yield superior imaging performance [60]. The interferogram is captured using a high-speed spectrometer (Cobra S-800, Wasatch Photonics, USA) connected to a frame grabber (PCIe-1429, National Instruments, USA). The same type of microscope objective (MY10X-803, Mitutoyo America Corporation, USA) is used both in the sample arm and in the reference arm to match the dispersion. A reflective collimator (RC12FC-P01, Thorlabs, USA) is coaxially aligned with the sample arm objective for optimized lateral resolution. For the PAM subsystem, a pulsed laser at 532 nm (SPOT, Elforlight, UK) is used as the excitation source. We set the repetition rate of the excitation source at 25 kHz in all our experiments, which is the highest pulse repetition rate supported by the onboard generator. Detection of the photoacoustic signal is by a customized focused ring transducer with a central opening of 3.81 mm in diameter, a central frequency of 35 MHz, an element size of 11.17 mm, and a focal length of 8.5 mm. At the bottom of the central clearance of the ring transducer, a circular glass piece with a thickness of 300 μm was secured to enable consistent light beam transmission through the acoustic couplant to the sample. The thickness of the active part of the ring transducer is 1.9 mm, yielding a working distance of 6.6 mm. To optimize confocal alignment for PAM, a translational mount (CXYZ05A/M, Thorlabs, USA) is used to fine tune the position of the ring transducer with respect to the microscope objective. The whole scanning unit for OC-PAM, composed of the collimator, the microscope objective, and the ring transducer, is mounted to a 3D printed structure that is in turn bolted to the voice coil actuator carriage. To optimize the stability of the scanning unit during fast scanning, the center of gravity of the whole scanning unit is matched to the top plane of the voice coil stage carriage. Figure 3(a) shows the schematic of the OC-PAM system. The coaxial alignment is illustrated in figure 3(b). To present the imaging head better, a cutaway view for the transducer, the glass window, the optical beam and the acoustic wave is shown in figure 3(c). As a supplement to figures 3(a), figure 3(d) shows a mostly 2D schematic of the system.

When the OCT subsystem is engaged, the camera is set to synchronization mode 2, in which the line camera makes a measurement whenever a trigger signal is received. When the PAM subsystem is engaged, the photoacoustic signal passes through a preamplifier (AU-1525, Miteq, USA) before being acquired by the FPGA whose sampling rate is hardwired to be 3.2 GS/s. Due to the excessively high sampling rate, the acquired data is down-sampled temporally by averaging by a factor of 8 onboard the FPGA. The employed Lissajous trajectory obviates the concept of B-scans. The A-lines in the OCT mode will be recorded according to the external or internal trigger source, whereas the A-lines in the PAM mode purely depends on the timing of the pulse from the excitation laser. Because the two axes'

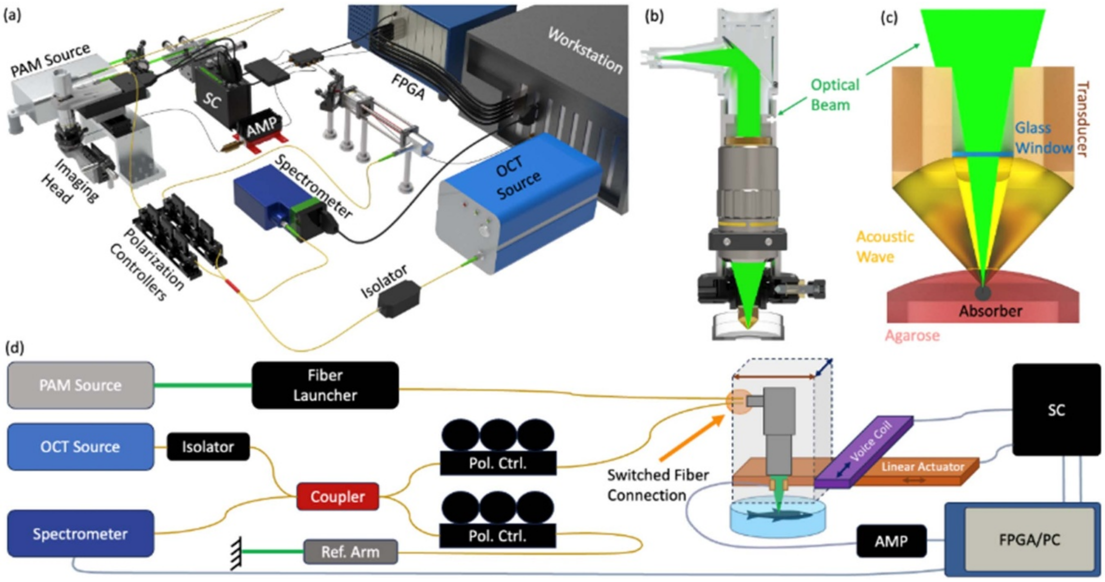

Figure 3. (a) 3D visualization of the OC-PAM system. (b) Cutaway view of the imaging head. (c) Enlarged view of the transducer-objective assembly. Green volume represents geometric visualization of the light exiting the objective. Yellow volume represents the space through which acoustic waves gathered by transducer are propagating. Pink volume represents agarose holding the sample. (d) Schematic of the OC-PAM system. AMP—amplifier, AC—axis controller, SC—stage controller, Pol. Ctrl.—polarization controller.

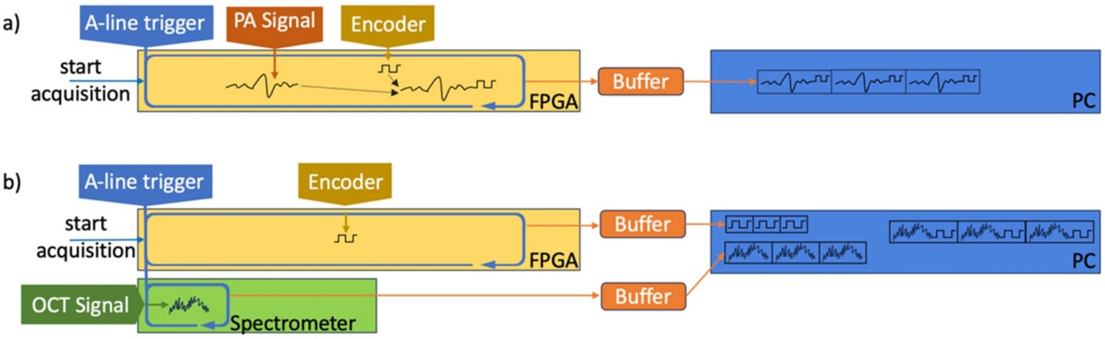

Figure 4. Position-data recombination schemes for (a) PAM signal, and (b) OCT signal.

encoders send real-time precise location information to the FPGA, which samples the encoder signals at a rate of 80 MHz, and that the same FPGA samples the photoacoustic signals upon triggering, each photoacoustic signal is appended with a header indicating the location. The OCT signal, however, cannot be directly tagged with position by FPGA since the OCT interferogram is not recorded by it. To solve this issue, the A-line triggers for OCT are sent through the FPGA, so that each interferogram can be tagged with the A-line trigger's timestamp before image reconstruction. The synchronization is graphically illustrated in figure 4.

2.3. Image reconstruction

The Lissajous pattern combined with constant frequency triggering creates a nonrectilinear map of measurement points. In order to display the image, a rectilinear grid of signal values needs to be calculated. When the total A-line count is less than 1 million, interpolation is handled by a Python subroutine. This script, utilizing 2D linear interpolation function from SciPy, is called by the main LabVIEW program during the acquisition software runtime. Because Python interpreters are not optimized for highly parallelized computation, when the total A-line count is equal to or larger than 1 million (typically more than 5 million, depending on the FOV), reconstructions are handled by a code written in MATLAB. This code is run post-acquisition, with multiple 2D layers being interpolated at the same time.

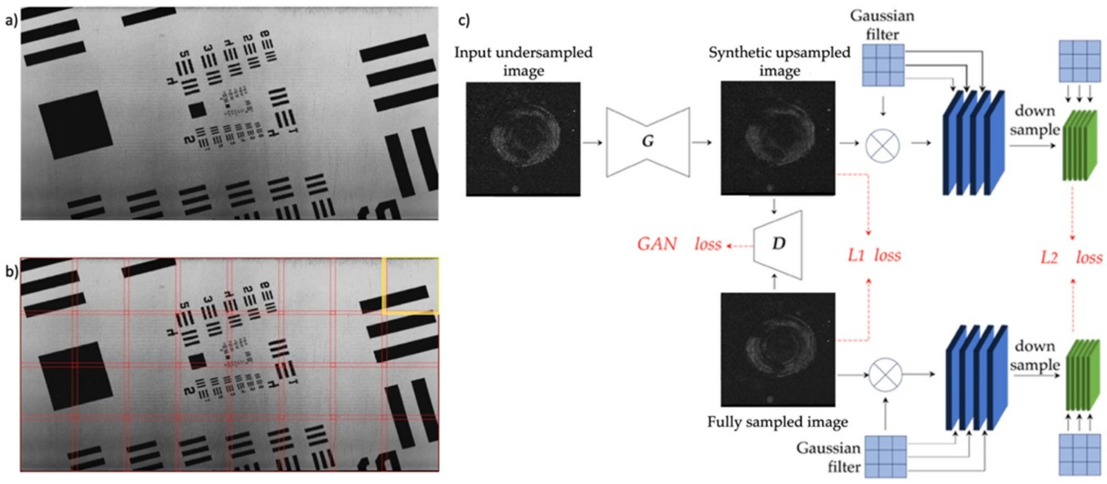

Figure 5. (a) Example of fully sampled picture before segmentation. (b) Fully sampled image divided into sub-images used for training the GAN model. Red lines indicate outlines of sub-images. Bright-yellow upper right line indicates a single sub-image with transparent yellow showing overlapping regions with neighboring sub-images. (c) Schematic of the GAN model training process.

2.4. Upsampling

The Lissajous trajectory inherently generates a sparse scanning pattern covering the whole FOV early in the scanning process. Data gathered in this period of the acquisition forms a good starting point for upsampling algorithms, which can provide an enhanced image from the sparsely acquired data much quicker than finishing the scan, especially for large images. This can be leveraged for significant shortening of acquisition time while maintaining a comparable image quality. A generative adversarial network (GAN) was employed to provide upsampled images when only undersampled images were given in input. In particular, to generate the training and the test sets, the same zebrafish and USAF resolution target were scanned using a different number of scanning points: 15%, 30%, 45% and fully sampled. The 15% and 45% images were employed as the training set, with fully sampled images representing the ground truth. The 30% scans were employed as the test set. For the GAN model, a Pyramidal Pix2Pix architecture, which leverages a multiresolution design for enhanced image generation was employed [61]. The generator uses an attention-UNet architecture with self-attention mechanisms to capture long-range dependencies and better preserve global image structure. The generator produces multi-resolution outputs, maintaining both fine details and overall characteristics, and the discriminator employs a patch-based approach. The loss function incorporates three components:

1. An adversarial (GAN) loss (figure 5(c)) to align the distributions of real and generated images;
2. A full-resolution L1 pixel loss (figure 5(c)), weighted by 25, to ensure pixel-level accuracy;
3. An L2 representation matching loss (figure 5(c)) weighted by 25 to match discriminator features, promoting perceptual similarity.

The overall objective function of the employed Pyramidal GAN (L_{Pyr}) is defined as:

$$L_{\mathrm{Pyr}}(G,D) = L_{\mathrm{GAN}}(G,D) + l_1 L_1(G) + l_2 L_2(G)$$

where:

$$L_{\mathrm{GAN}}(G,D) = E_y[\log\mathrm{D}(y)] + E_x[\log(1 - D(G(x)))]$$

$$L_1(G) = E_{\{x,y\}}[\|y - G(x)\|_1]$$

$$L_2(G) = E_{\{x,y\}}\left[\|D_{\mathrm{feat}}(y) - D_{\mathrm{feat}}(G(x))\|_2^2\right]$$

L_{GAN} is the adversarial loss; L_1 is the pixel-wise loss; and L_2 is the feature matching loss. The λ terms are the respective weighting factors. This multi-scale adversarial training framework facilitates the synthesis of upsampled sound images that closely mimic the characteristics of the sampled image. The

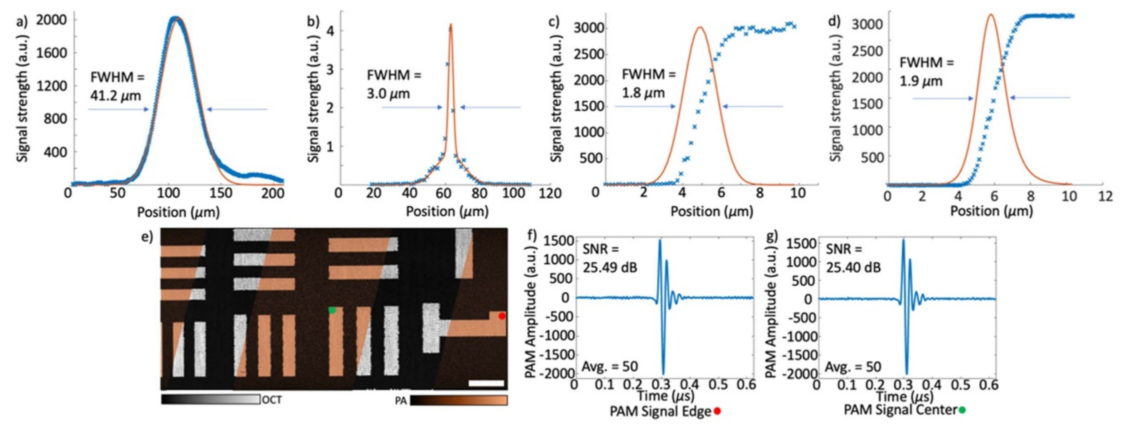

Figure 6. (a) PAM axial resolution measurement result. Blue: raw data; orange: Gaussian fit. (b) OCT axial resolution measurement result. Blue: raw data; orange: Gaussian fit. (c) PAM lateral resolution measurement result. Blue: raw data; orange: fitted edge spread function. (d) OCT lateral resolution measurement result. Blue: raw data; orange: fitted edge spread function. (e) OC-PAM imaging results of USAF 1951 resolution target showing group −1 elements 1, 2, and 3, indicating coregistration of the two modalities as well as the maximum FOV (11.8 mm × 25.2 mm). (f) A-line taken from the edge of the FOV marked with the red dot. (g) A-line taken from the central part of the FOV marked with the green dot.

model was trained for 200 epochs with alternating generator and discriminator updates. The input size was set to 512 × 512 pixels and generator weights were saved every 5 epochs, using instance normalization. Since the acquisitions were larger than the input size (figure 5(a)), the images were divided into overlapping patches with minimal number of sub-images (figure 5(b)) needed to cover the whole image. The best epoch was chosen based on the loss value. The model was trained on a workstation equipped with an NVIDIA RTX3090 with 24 GB of memory. The inference time (i.e., the time required to generate the synthetic patch) is approximately 30 ms.

2.5. Zebrafish preparation

We chose casper zebrafish (mpv^{a9}, mitfa$^{w2/w2}$) for its low number of melanocytes [62]. Five days post fertilization (dpf) larvae were provided by St. Anna Children's Cancer Research Institute prior to imaging. Zebrafish larvae were anesthetized in a 1% tricaine solution. In order to prevent movement of the fish by water currents induced by the moving transducer, the larvae were embedded in 1.2% low melt agarose (Agarose A2576-5G, Sigma-Aldrich, USA) on a glass-bottom petri dish, which was placed on a vertical stage (MT1, Thorlabs, USA) for height adjustment and an angular stage (PY003, Thorlabs, USA) for rotation adjustment. The fish were monitored under a stereomicroscope (DMBZ SD2, Brunel Microscopes, UK) equipped with a camera (DFK 33UX178, The Imaging Source, USA) to assess the presence of a heartbeat and proper anesthetization before and after OC-PAM imaging.

3. Results

3.1. Maging system characterization

The lateral resolution of the OC-PAM system is measured by imaging a sharp edge of a USAF 1951 resolution target (R1DS1P, Thorlabs, USA). The axial resolution of PAM is directly calculated using the A-line signal generated by the 1 μm chrome coating of the resolution target to be 41.2 μm, which is in agreement with the theoretical value for a transducer with a central frequency of 35 MHz. The axial resolution of OCT is calculated to be 3 μm in air, based on the A-line signal acquired from imaging a silver mirror (CM254-019-P01, Thorlabs, USA). Figures 6(a)–(d) shows the measurement results for the axial and lateral resolutions of both modalities of the system. The sensitivity of the OCT modality is measured to be 90.22 dB.

To show the uniform sensitivity and image quality over a large FOV, we used $f_x = 5.73$ Hz, $f_y = 0.372$ Hz, $A = 11.8$ mm, $B = 25.2$ mm to image a large resolution target (R3L3S1P, Thorlabs, USA). A safety margin of 0.1 mm for the FOV was left in all sides to avoid possible mechanical shocks caused by motion controller overshoots. The resulting images acquired with both OCT and PAM modalities are shown in figure 6(e). The movement frequencies were lowered due to inability of the actuators to maintain higher frequencies over long ranges. The orange-colored parts in figure 6(e) are reconstructed from PAM, whereas the white colored parts are reconstructed from OCT. The seamless transition of the two half images show that the two modalities can be perfectly coregistered. The raw photoacoustic signal

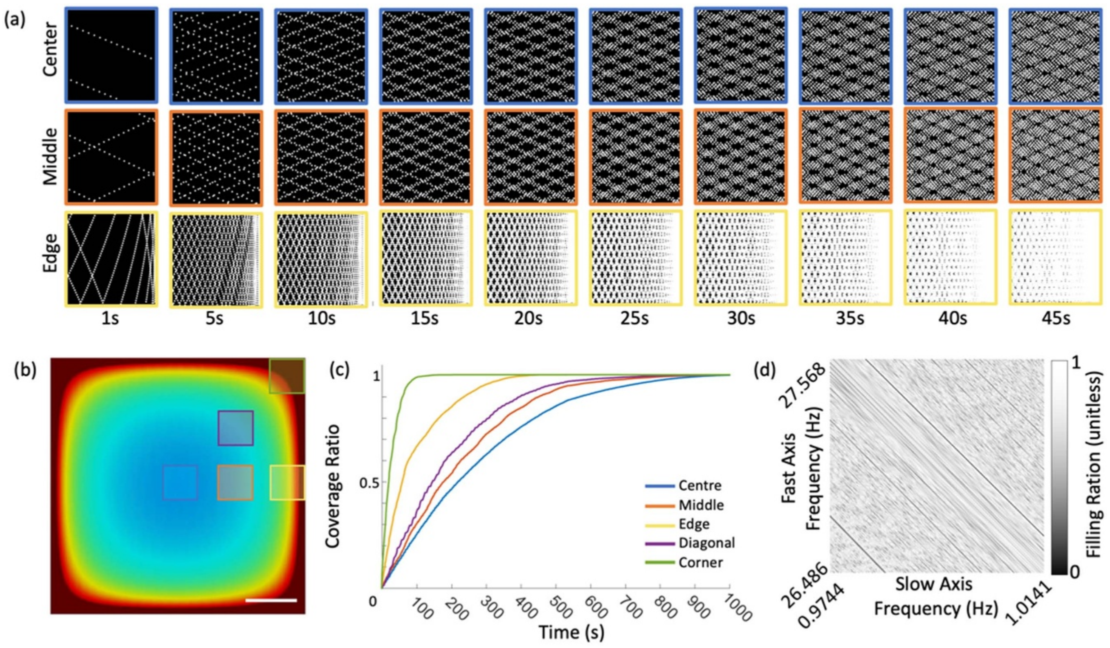

Figure 7. (a) Simulation of the scanning pattern changes in the first 45 s. Images represent 50 μm × 50 μm subsections of FOV at different locations. The pixel size is 0.1 μm × 0.1 μm. White color represents pixels which have been scanned over at least once with circular 2 μm spot. (b) Indication of positions of subsections in figure (a). The squares have been enlarged for presentation purposes. Centers of the squares maintain real positions. Scalebar: 1 mm. (c) Change of area FR in time during simulated scanning. (d) Plot of FR reached in the typical zebrafish FOV after 60 s of scanning with different fast and slow axis frequency pairs with simulated 2 μm resolution.

from point 1 (red dot on figure 6(e)) and point 2 (green dot on figure 6(e)) are plotted in figures 6(f) and (g). Comparing the two plots, it is clear that the signal to noise ratio (SNR) stays the same across all the regions in the FOV.

As mentioned in the previous sections, there is a direct, non-linear relation between movement frequencies and FR. Since larger FOV puts more strain on actuators at the same frequency parameters, different FOVs use different sets of frequencies. Figure 7(d) shows the FR reached after 60 s for an FOV of 0.5 mm × 4 mm (typical for zebrafish FOV) for different frequency pairs. The diagonal dark lines indicate frequency pairs where Lissajous pattern collapses into low density trajectory. The bright sections of the graph show the combinations which create desired high-density patterns, but there is no clear distribution of where they appear, making analytical selection of the best pair impossible. The time-emulating simulation further shows how the FR changes in time at different speed in different regions of the FOV (figures 7(a)–(c)). Edge (yellow) and corner (green) plots in figure 7(c) indicate that the outer regions of the FOV are fully sampled long before the central regions can reach an FR high enough to reconstruct a viable image. This further warrants the necessity for AI-based upsampling, which could use information from outer parts to improve interpolation in the central regions.

3.2. OC-PAM imaging of the zebrafish

In order to demonstrate the ability of the system to image biological samples with both modalities, we used 5 dpf zebrafish larvae embedded in agarose. The following parameters were used for the imaging: $f_x = 11.09$ Hz , $f_y = 0.569$ Hz, FOV $= 0.94$ mm × 3.815 mm. The pulse energy of the excitation laser at the focal plane was set to 80 nJ measured in air, which is in line with the fluence used in other PAM systems for zebrafish larva imaging [38]. The OCT delivered continuous power equal to 47.3 μW adjusted for 840 nm. The acquisition of a single volume took 4.1 min for both PAM and OCT. The imaging results of OCT, PAM, and OC-PAM are given in figure 8. As a comparison, classical raster-scanning over the same FOV with the same hardware would have taken 5.8 min, while also requiring additional 0.2 mm margins for acceleration and deceleration of the imaging head. The proposed Lissajous trajectory represents 29.3% acquisition time decrease compared to the traditional raster-scanning pattern in this scenario. Details of this comparison are given in the supplementary materials.

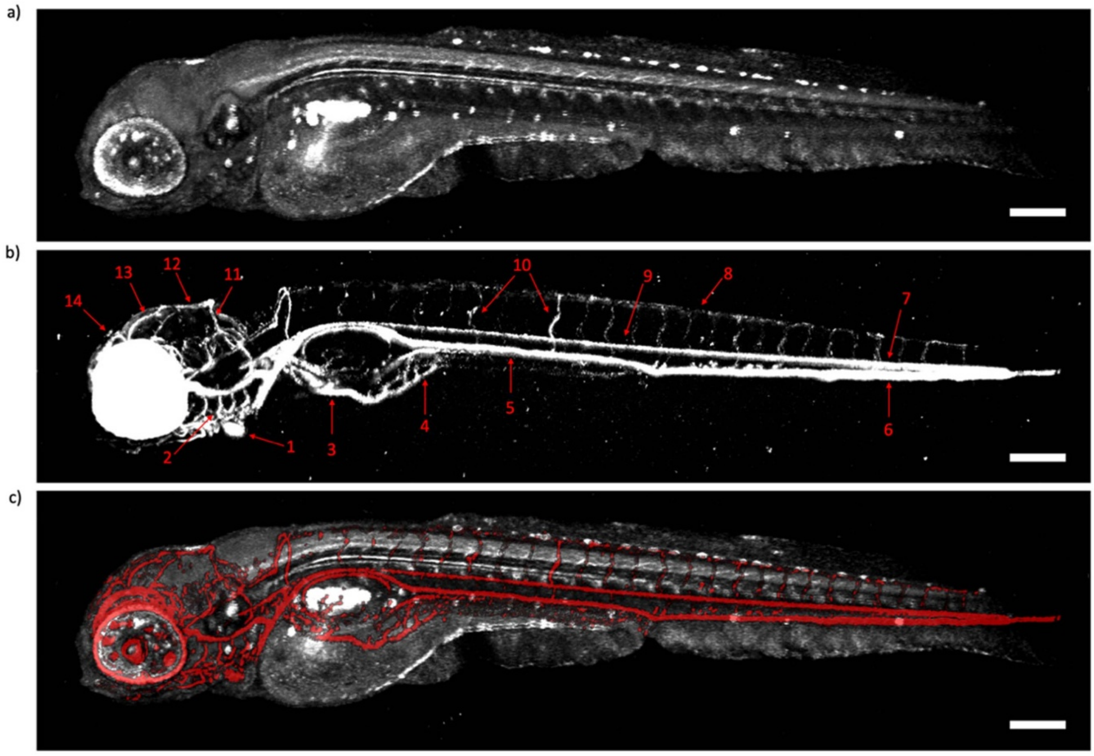

Figure 8. OC-PAM imaging results of a 5 dpf zebrafish larva. (a) Maximum intensity projection (MIP) OCT result. (b) MIP PAM result showing: (1) heart (2) aortic arches (3) hepatic portal vein (4) subintestinal vein (5) posterior cardinal vein (6) caudal vein (7) caudal artery (8) dorsal longitudinal anastomotic vessel (9) dorsal aorta (10) intersegmental vessels (11) posterior cerebral vein (12) dorsal longitudinal vein (13) mesencephalic vein (14) anterior cerebral vein. (c) Overlaid OC-PAM MIP image. PAM image (red) has been additionally treated with vessel filters. Video rendering of the 3D OC-PAM result of the fish can be found in the supplementary material. Scalebar: 200 μm.

3.3. Upsampling validation

Figure 9 demonstrates the results of the upsampling algorithm. It is shown to be capable of generating an image which is comparable with the one from the full acquisition. Low FR in the center of the FOV in the undersampled image (figure 9(b)) results in increased noise by traditional interpolation, which is not present in the upsampled image (figure 9(c)). Apart from visual impression of an overall improved quality, the results have been deemed satisfactory by a comparison of visual clarity (figures 10(a)–(d)) of more important subsections of the images and by comparison of the calculated sharpness of images (figures 10(f)–(g)). Both groups (biological and synthetic samples) have shown significant improvement of sharpness after upsampling was performed on the undersampled image. In both groups, the fully sampled images had higher sharpness than the upsampled ones, which was expected, as sparse sampling might completely miss small details, which upsampling would have no information about. This is especially visible in intersegmental vessels in figure 9, which are less visible in the upsampled image as compared to those in the image of full acquisition. The network was taught based on images of various FOVs, which utilized various sets of f_x and f_y, as high frequencies suitable for small FOVs could not be sustained at significantly larger FOVs. Those requirements prevented the model from overfitting to the frequency-pair-specific distribution of sampled points. The sizes of the training and test set for each imaging object are listed in figure 10(e). The trained model is also independent on the image modality, and can be used for both PAM and OCT images.

4. Discussion

The OC-PAM system using the Lissajous trajectory has several advantages compared to other types of configurations. Using a focused transducer and the coaxial alignment of optics and acoustics, the spatial resolution is uniform throughout the whole FOV because the focal plane shows no distortion and does not experience aberrations. The configuration allows the use of high numerical aperture objectives, which in this case yields a lateral resolution of 1.8 μm. Limited only by the travel range of the stages, the achievable FOV is much larger than that of other configurations. In this study, due to the relatively high payload, we limited f_x to be 11.09 Hz to avoid overstraining the voice coil actuator. However, this

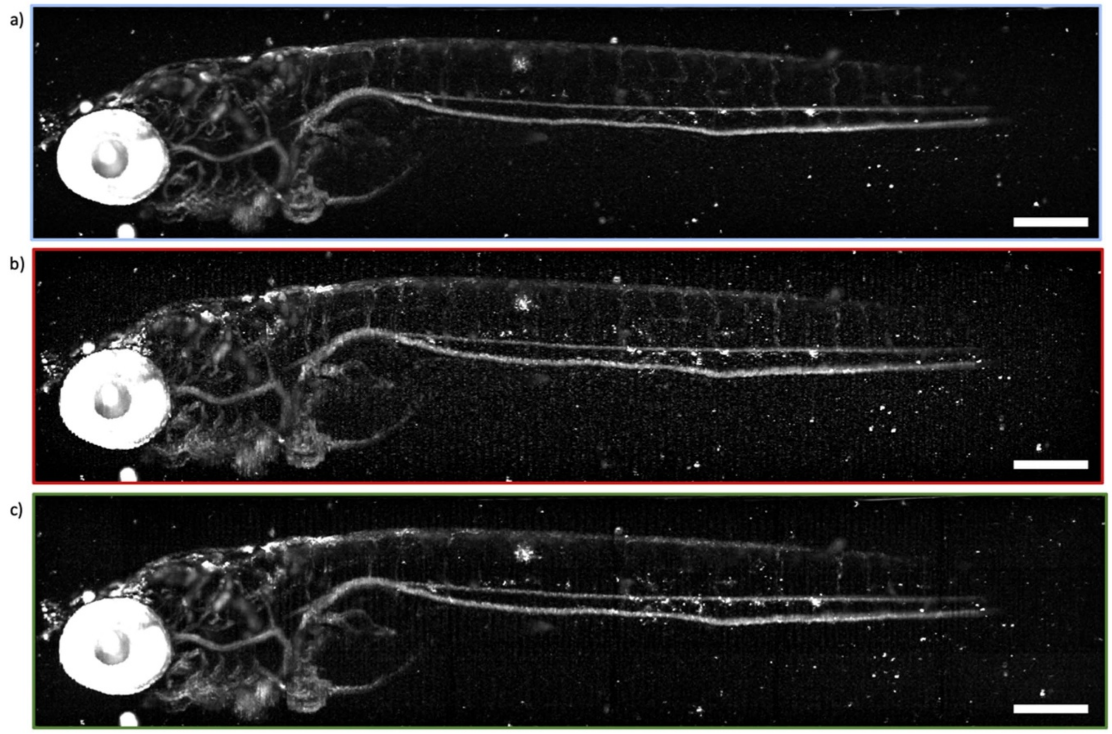

Figure 9. Comparison of fully sampled, undersampled and upsampled PAM images of a zebrafish larva. (a) Fully sampled image. (b) Image reconstructed from 30% of data by interpolation. (c) Image upsampled by AI from 30% of the data. Scalebar: 200 μm. Colored outlines of images are consistent with those in figure 10.

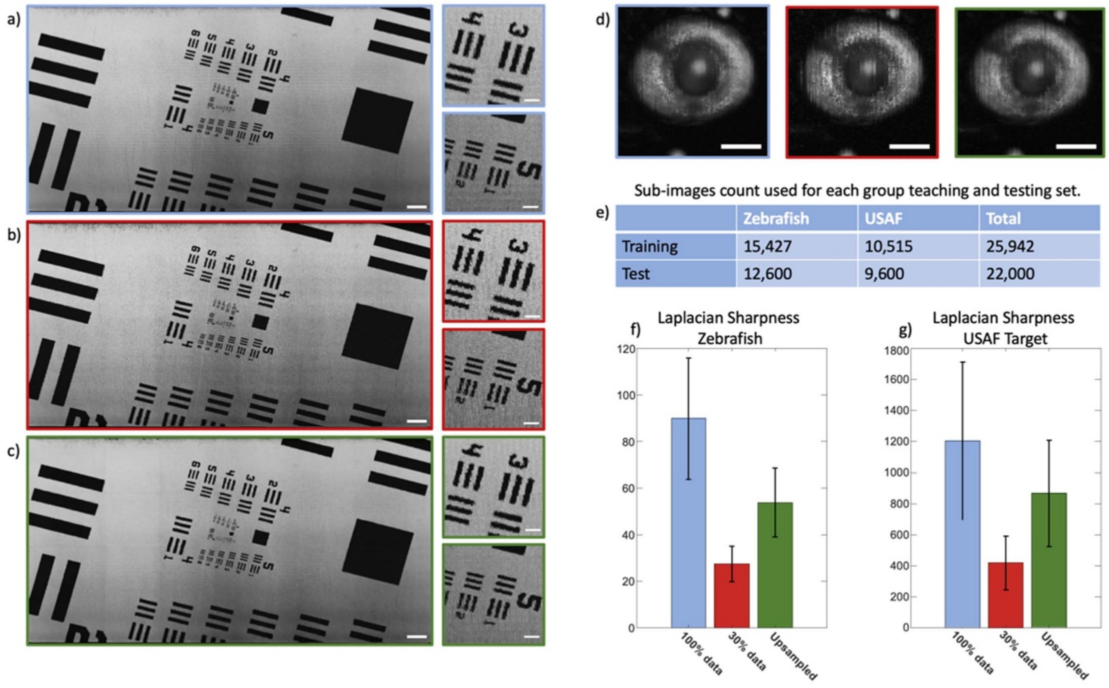

Sub-images count used for each group teaching and testing set.

	Zebrafish	USAF	Total
Training	15,427	10,515	25,942
Test	12,600	9,600	22,000

Figure 10. Comparison of original, undersampled, and upsampled PAM images. (a) Fully sampled image of a USAF 1951 target with 2 sub-images (blue outline). (b) Image from 30% acquisition time with 2 sub-images (red outline). (c) Upsampled image of the target with 2 sub-images (green outline). (d) Fully sampled (blue outline), 30% acquisition time (red outline), and upsampled (green outline) images of 5 dpf zebrafish eye. (e) Table with numbers of sub-images used for training and testing the upsampling algorithm. (f) Comparison of Laplacian sharpness of fully sampled, undersampled, and upsampled images of zebrafish larvae. (g) Comparison of Laplacian sharpness of fully sampled, undersampled, and upsampled images of the USAF 1951 target. Scalebars: Large USAF 1951–200 μm, USAF 1951 sub-images—50 μm, zebrafish eyes—100 μm.

payload can be significantly reduced by using a fiber connected GRIN lens [63, 64] to replace the reflective collimator and the objective. In the current setup, the objective, collimator, and the holding structure weigh 708.17 g. If we use a fiber coupled GRIN lens to fill in the central clearance of the ring transducer, the total payload for the voice coil actuator can be reduced to 200 g. Assuming a 4 mm × 1 mm FOV and both axes using voice coil actuators, this reduced payload will allow $f_x = 25.011$ Hz and $f_y = 24.943$ Hz, which in turn yield an image acquisition time of 102 s assuming100 kHz pulse repetition rate with an FR of 90.1%. This image acquisition time can be even further reduced to 34.1 s when the proposed upsampling algorithm is used. While the data shown here are preliminary and could be subject to overfitting due to the limited dataset, the initial results are very promising and show how the model is able to effectively learn the upsampling process through the pixel-to-pixel analysis.

In this work, the two orthogonal directions are scanned in sinusoidal trajectories, leading to non-equidistant spacing of sampled points and much of the image acquisition time is used to finish scanning the central part of the FOV with enough points, but minimizes rapid changes in acceleration and their negative impact on precisely aligned elements. Using triangular wave forms, researchers have demonstrated a much more uniform Lissajous-like scanning pattern in stimulated Raman scattering imaging [65]. This modified Lissajous-like pattern not only shortens the image acquisition time, but may also enable much faster image reconstruction. Another extension of the current 2D Lissajous scanning trajectory is to extend it to a volumetric Lissajous scanning trajectory. It has been demonstrated that, by scanning the z-focus using an ultrasound driven liquid lens, the 3D Lissajous scanning trajectory achieved 30 times the native depth of field of the objective in a confocal microscopy setup [66]. When implemented in OC-PAM, a 3D Lissajous pattern will allow sharper images to be acquired for different excitation wavelengths as well as the extension of the depth of field.

While the demonstrated 4.1 min per zebrafish imaging time may not be fast enough to capture rapid changes in the sample, studies focusing on dynamic processes rarely need whole body images. For instance, for functional studies such as the investigation of brain vasodilation, an FOV covering the brain region is sufficient [51]. As a quick reference, assuming an FOV of 1 mm × 1 mm, an image size of 512 pixel × 512 pixel, and upsampling using 30% data, the acquisition time will be 8 s. When faster PAM sources and faster voice coil actuators are used, it is possible that the Lissajous trajectory equipped with upsampling can finish a 1 mm^2 FOV scan within just a second. Holding the potential for functional imaging enabled by fast speed, this OC-PAM system also holds potential for functional imaging enabled by endogenous and exogenous contrast agents. Currently, the implementation of mode switching requires changing fibers, which makes mode changing between OCT and PAM relatively cumbersome. Similarly, using different excitation wavelengths for PAM requires coupling different light sources into the collimator in the imaging head, which makes spectroscopic PAM time-consuming. In addition to use muti-core fibers, the use of supercontinuum sources [67, 68] and multi-color fiber laser sources [69] may enable easier spectroscopic PAM in the dual modal OC-PAM configuration.

The setup used in this work consists of a ring transducer and a 10X objective for PAM as well as a 3 superluminescent diode (SLED) OCT system. The platform, however, is compatible with a wide range of other components depending on the application needs. For example, instead of using a ring transducer, either the typical beam combiner configuration for PAM [70] or a transparent transducer [71] may be easily implemented and still allowing dual modal OC-PAM operation. Other types of spectral domain OCT systems can also be used. Depending on the resolution need, objectives with either higher or lower magnification ratios may be used. When deep imaging depth is the priority, this OR-PAM setting can be replaced with an acoustic resolution PAM configuration, too. The real-time position tracking also allows the system to be used with any pulsed light source, regardless of the existence of jitter. This makes it a very useful platform for testing novel light sources, as the only requirement for excitation light is to be coupled into an optical fiber.

As a system specially designed for zebrafish imaging, the FOV presented in figure 9 is sufficient for individual fish imaging. When there is a need for high-throughput application, the FOV can be digitally divided into 75 separate 4 mm × 1 mm larva-sized sub-FOVs, enabling a 'fire-and-forget' approach to multimodal microscopy. This large-area imaging capability is not demonstrated in the present study, primarily due to the challenge of consistently embedding all larvae in the right lateral decubitus position such that they lie within a flat focal plane. However, when 3D Lissajous patterns are achieved, batch imaging may become feasible. In future works, AI-based fish detection could be applied to a coarse overview scan of the full FOV to automatically allocate sub-FOVs, thereby further reducing human intervention.

5. Conclusion

This work introduces a novel OC-PAM implementation that features a large FOV, uniformly high sensitivity, and relatively high speed. The coexisting of these unique features can enable new zebrafish imaging applications using OC-PAM. Furthermore, accurate real-time position encoding makes equidistance scanning irrelevant, which means that the OC-PAM system is inherently immune to laser jittering. This unique advantage significantly loosens the requirement on PAM sources, therefore allowing more wavelengths and more cost-effective lasers to be used in the future. Although the imaging speed is still lower than that of scanning mirror-based systems, the AI-assisted upsampling algorithm reduces the total image acquisition time significantly without significantly deteriorating the image fidelity. Although only demonstrated in zebrafish embryo imaging in this work, with minor adaptations, the system can also be used for biomedical research using other model organisms.

Data availability statement

The data cannot be made publicly available upon publication because they are not available in a format that is sufficiently accessible or reusable by other researchers. The data that support the findings of this study are available upon reasonable request from the authors.

Funding

This work is funded by the H2020 FETOPEN project SWIMMOT with Grant agreement ID 899612 and the H2020 ICT project REAP with Grant agreement ID 101016964. M. Liu was funded by H2020 MSCA project SkinOptima with Grant agreement ID 894325.

Conflict of interest

The authors declare no conflicts of interest.

Author contributions

Lukasz Bugyi 0009-0009-9722-9445
Conceptualization (lead), Data curation (supporting), Formal analysis (lead), Investigation (lead), Methodology (lead), Software (lead), Validation (lead), Visualization (equal), Writing – original draft (equal)

Nicole Schmitner 0009-0009-3036-866X
Resources (lead), Writing – review & editing (equal)

Robin A Kimmel 0000-0002-9283-1252
Resources (equal)

Dirk Meyer 0000-0002-4020-4484
Resources (equal)

Qifa Zhou 0000-0003-1527-3020
Resources (equal)

Richard Haindl 0000-0003-3471-0986
Conceptualization (supporting)

Massimo Salvi 0000-0001-7225-7401
Software (supporting)

Giulia Rotunno 0000-0003-4239-5816
Visualization (supporting)

Kristen M Meiburger 0000-0002-7302-6135
Software (equal)

Martin Distel 0000-0001-5942-0817
Resources (supporting)

Caterina Sturtzel 0000-0003-1002-5634
Resources (supporting)

Yi Yuan 0000-0002-8951-810X
Conceptualization (supporting)

Mengyang Liu 0000-0002-8862-5966
Project administration (equal), Resources (equal), Supervision (equal), Writing – original draft (equal), Writing – review & editing (equal)

References

[1] Choi T-Y, Choi T-I, Lee Y-R, Choe S-K and Kim C-H 2021 Zebrafish as an animal model for biomedical research *Exp. Mol. Med.* **53** 310–7

[2] Bashirzade A A *et al* 2022 Modeling neurodegenerative disorders in zebrafish *Neurosci. Biobehav. Rev.* **138** 104679

[3] Wang L, Liu F, Fang Y, Ma J, Wang J, Qu L, Yang Q, Wu W, Jin L and Sun D 2023 Advances in zebrafish as a comprehensive model of mental disorders *Depress Anxiety* **2023** 6663141

[4] Levraud J-P, Rawls J F and Clatworthy A E 2022 Using zebrafish to understand reciprocal interactions between the nervous and immune systems and the microbial world *J. Neuroinflamm.* **19** 170

[5] Salmi T M, Tan V W T and Cox A G 2019 Dissecting metabolism using zebrafish models of disease *Biochem. Soc. Trans.* **47** 305–15

[6] Patton E E, Zon L I and Langenau D M 2021 Zebrafish disease models in drug discovery: from preclinical modelling to clinical trials *Nat. Rev.* **20** 611–28

[7] Høgset H *et al* 2020 In vivo biomolecular imaging of zebrafish embryos using confocal Raman spectroscopy *Nat. Commun.* **11** 6172

[8] Lam P-Y, Fischer R S, Shin W D, Waterman C M and Huttenlocher A 2014 Spinning disk confocal imaging of neutrophil migration in zebrafish *Neutrophil Methods and Protocols* ed M T Quinn and F R DeLeo (Humana Press) pp 219–33

[9] Ahrens M B, Li J M, Orger M B, Robson D N, Schier A F, Engert F and Portugues R 2012 Brain-wide neuronal dynamics during motor adaptation in zebrafish *Nature* **485** 471–7

[10] Huisken J, Swoger J, Del Bene F, Wittbrodt J and Stelzer E H K 2004 Optical sectioning deep inside live embryos by selective plane illumination microscopy *Science* **305** 1007–9

[11] He R, Xu Y, Zhang L, Ma S, Wang X, Ye D and Ji M 2017 Dual-phase stimulated Raman scattering microscopy for real-time two-color imaging *Optica* **4** 44–47

[12] LeBert D C, Squirrell J M, Huttenlocher A and Eliceiri K W 2016 Chapter 3—second harmonic generation microscopy in zebrafish *Methods in Cell Biology* vol 133, ed H W Detrich, M Westerfield and L I Zon (Academic) pp 55–68

[13] Morizet J, Ducourthial G, Supatto W, Boutillon A, Legouis R, Schanne-Klein M-C, Stringari C and Beaurepaire E 2019 High-speed polarization-resolved third-harmonic microscopy *Optica* **6** 385–8

[14] Toms M, Tracey-White D, Muhundhakumar D, Sprogyte L, Dubis A M and Moosajee M 2017 Spectral domain optical coherence tomography: an *in vivo* imaging protocol for assessing retinal morphology in adult zebrafish *Zebrafish* **14** 118–25

[15] Weber A, Hochmann S, Cimalla P, Gärtner M, Kuscha V, Hans S, Geffarth M, Kaslin J, Koch E and Brand M 2013 Characterization of light lesion paradigms and optical coherence tomography as tools to study adult retina regeneration in zebrafish *PLoS One* **8** e80483

[16] Lin Y, Xiang X, Chen T, Mao G, Deng L, Zeng L and Zhang J 2019 In vivo monitoring the dynamic process of acute retinal hemorrhage and repair in zebrafish with spectral-domain optical coherence tomography *J. Biophoton.* **12** e201900235

[17] Bozic I, Li X and Tao Y 2018 Quantitative biometry of zebrafish retinal vasculature using optical coherence tomographic angiography *Biomed. Opt. Express* **9** 1244–55

[18] Huckenpahler A L, WILK M A, Cooper R F, Moehring F, Cooper B A, Cooper J and Collery R F 2016 Imaging the adult zebrafish cone mosaic using optical coherence tomography *Visual Neurosci.* **33** E011

[19] Lapierre-Landry M, Huckenpahler A L, Link B A, Collery R F, Carroll J and Skala M C 2018 Imaging melanin distribution in the zebrafish retina using photothermal optical coherence tomography *Trans. Vis. Sci. Technol.* **7** 4

[20] Lichtenegger A *et al* 2022 Multicontrast investigation of in vivo wildtype zebrafish in three development stages using polarization-sensitive optical coherence tomography *J. Biomed. Opt.* **27** 016001

[21] Divakar Rao K, Upadhyaya P, Sharma M and Gupta P K 2012 Noninvasive imaging of ethanol-induced developmental defects in zebrafish embryos using optical coherence tomography *Birth Defects Res.* **95** 7–11

[22] Li K, Wang Y, Liu Y, Li W, Weng Z, Li H, He Y and Li Z 2022 Morphological characteristics of zebrafish's yolk sac for malformation based on orthogonal-polarization-gating optical coherence tomography *J. Biophoton.* **15** e202200098

[23] Alam Z and Poddar R 2022 An *in-vivo* depth-resolved imaging of developing zebrafish microstructure and microvasculature using swept-source optical coherence tomography angiography *Opt. Lasers Eng.* **156** 107087

[24] Xiang X *et al* 2022 Study on promoting regeneration of zebrafish skull by phycocyanin characterized by in vivo optical coherence tomography *J. Biophoton.* **15** e202100333

[25] Asani P C, Alam Z and Poddar R 2023 Exploring the impact of PVC and PVA microplastics on zebrafish tissue using multi-spectral imaging, Optical coherence tomography (OCT) and biospeckle OCT (bOCT) *Chemosphere* **341** 140088

[26] Ma R, Distel M, Deán-Ben X L, Ntziachristos V and Razansky D 2012 Non-invasive whole-body imaging of adult zebrafish with optoacoustic tomography *Phys. Med. Biol.* **57** 7227

[27] Huang N, Guo H, Qi W, Zhang Z, Rong J, Yuan Z, Ge W, Jiang H and Xi L 2016 Whole-body multispectral photoacoustic imaging of adult zebrafish *Biomed. Opt. Express* **7** 3543–50

[28] Liu Y, Li D and Yuan Z 2016 Photoacoustic tomography imaging of the adult zebrafish by using unfocused and focused high-frequency ultrasound transducers *Appl. Sci.* **6** 392

[29] Vetschera P *et al* 2023 Beyond early development: observing zebrafish over 6 weeks with hybrid optical and optoacoustic imaging *Laser Photon. Rev.* **17** 2200846

[30] Liu M, Schmitner N, Sandrian M G, Zabihian B, Hermann B, Salvenmoser W, Meyer D and Drexler W 2013 In vivo three dimensional dual wavelength photoacoustic tomography imaging of the far red fluorescent protein E2-Crimson expressed in adult zebrafish *Biomed. Opt. Express* **4** 1846–55

[31] Zhu L, Li L, Gao L and Wang L V 2014 Multiview optical resolution photoacoustic microscopy *Optica* **1** 217–22

[32] Omar M, Rebling J, Wicker K, Schmitt-Manderbach T, Schwarz M, Gateau J, López-Schier H, Mappes T and Ntziachristos V 2017 Optical imaging of post-embryonic zebrafish using multi orientation raster scan optoacoustic mesoscopy *Light Sci. Appl.* **6** e16186

[33] Kneipp M, Estrada H, Lauri A, Turner J, Ntziachristos V, Westmeyer G G and Razansky D 2015 Volumetric tracking of migratory melanophores during zebrafish development by optoacoustic microscopy *Mech. Dev.* **138** 300–4

[34] Chen Q, Jin T, Qi W, Mo X and Xi L 2017 Label-free photoacoustic imaging of the cardio-cerebrovascular development in the embryonic zebrafish *Biomed. Opt. Express* **8** 2359–67

[35] Yang W, Wang W, Jing L and Chen S-L 2021 Label-free photoacoustic microscopy: a potential tool for the live imaging of blood disorders in zebrafish *Biomed. Opt. Express* **12** 3643–57

[36] Deng S *et al* 2021 An optical coherence photoacoustic microscopy system using a fiber optic sensor *APL Photonics* **6** 096103

[37] Haindl R *et al* 2017 Dual modality reflection mode optical coherence and photoacoustic microscopy using an akinetic sensor *Opt. Lett.* **42** 4319–22

[38] Haindl R *et al* 2020 Functional optical coherence tomography and photoacoustic microscopy imaging for zebrafish larvae *Biomed. Opt. Express* **11** 2137–51

[39] Ansari R, Zhang E Z, Desjardins A E and Beard P C 2018 All-optical forward-viewing photoacoustic probe for high-resolution 3D endoscopy *Light Sci. Appl.* **7** 75

[40] Preisser S, Rohringer W, Liu M, Kollmann C, Zotter S, Fischer B and Drexler W 2016 All-optical highly sensitive akinetic sensor for ultrasound detection and photoacoustic imaging *Biomed. Opt. Express* **7** 4171–86

[41] Hosseinaee Z, Tummon Simmons J A and Reza P H 2021 Dual-modal photoacoustic imaging and optical coherence tomography *Front. Phys.* **8** 616618

[42] Leitgeb R *et al* 2021 Enhanced medical diagnosis for doctors: a perspective of optical coherence tomography *J. Biomed. Opt.* **26** 100601

[43] Dadkhah A and Jiao S 2019 Optical coherence tomography-guided dynamic focusing for combined optical and mechanical scanning multimodal photoacoustic microscopy *J. Biomed. Opt.* **24** 1–6,6

[44] Dadkhah A and Jiao S 2020 Integrating photoacoustic microscopy, optical coherence tomography, OCT angiography, and fluorescence microscopy for multimodal imaging *Exp. Biol. Med.* **245** 342–7

[45] Dadkhah A, Zhou J, Yeasmin N and Jiao S 2019 Integrated multimodal photoacoustic microscopy with OCT- guided dynamic focusing *Biomed. Opt. Express* **10** 137–50

[46] Nguyen V P, Li Y, Zhang W, Wang X and Paulus Y M 2019 High-resolution multimodal photoacoustic microscopy and optical coherence tomography image-guided laser induced branch retinal vein occlusion in living rabbits *Sci. Rep.* **9** 10560

[47] Nguyen V-P, Li Y, Henry J, Zhang W, Aaberg M, Jones S, Qian T, Wang X and Paulus Y M 2020 Plasmonic gold nanostar-enhanced multimodal photoacoustic microscopy and optical coherence tomography molecular imaging to evaluate choroidal neovascularization *ACS Sens.* **5** 3070–81

[48] Song W, Wei Q, Liu T, Kuai D, Burke J M, Jiao S and Zhang H F 2012 Integrating photoacoustic ophthalmoscopy with scanning laser ophthalmoscopy, optical coherence tomography, and fluorescein angiography for a multimodal retinal imaging platform *J. Biomed. Opt.* **17** 0612061–7

[49] Varkentin A, Mazurenka M, Blumenröther E, Behrendt L, Emmert S, Morgner U, Meinhardt-Wollweber M, Rahlves M and Roth B 2018 Trimodal system for in vivo skin cancer screening with combined optical coherence tomography-Raman and colocalized optoacoustic measurements *J. Biophoton.* **11** e201700288

[50] Liu T, Wei Q, Wang J, Jiao S and Zhang H F 2011 Combined photoacoustic microscopy and optical coherence tomography can measure metabolic rate of oxygen *Biomed. Opt. Express* **2** 1359–65

[51] Tsytsarev V, Rao B, Maslov K I, Li L and Wang L V 2013 Photoacoustic and optical coherence tomography of epilepsy with high temporal and spatial resolution and dual optical contrasts *J. Neurosci. Methods* **216** 142–5

[52] Zhu X, Huang Z, Li Z, Li W, Liu X, Chen Z, Tian J and Li C 2020 Resolution-matched reflection mode photoacoustic microscopy and optical coherence tomography dual modality system *Photoacoustics* **19** 100188

[53] Liu M *et al* 2021 REAP: revealing drug tolerant persister cells in cancer using contrast enhanced optical coherence and photoacoustic tomography *J. Phys. Photon.* **3** 021001

[54] Cho S-W, Nguyen V T, DiSpirito A, Yang J, Kim C-S and Yao J 2024 Sounding out the dynamics: a concise review of high-speed photoacoustic microscopy *J. Biomed. Opt.* **29** S11521

[55] Wang L, Maslov K, Xing W, Garcia-Uribe A and Wang L 2012 Video-rate functional photoacoustic microscopy at depths *J. Biomed. Opt.* **17** 106007

[56] Wang L, Maslov K, Yao J, Rao B and Wang L V 2011 Fast voice-coil scanning optical-resolution photoacoustic microscopy *Opt. Lett.* **36** 139–41

[57] Tuma T, Lygeros J, Kartik V, Sebastian A and Pantazi A 2012 High-speed multiresolution scanning probe microscopy based on Lissajous scan trajectories *Nanotechnology* **23** 185501

[58] Kim J-B, Jeon J, Hwang K, Kim D and Jeong K-H 2021 Objective-lens-free confocal endomicroscope using Lissajous scanning lensed-fiber *J. Opt. Microsyst.* **1** 034501

[59] Hwang K *et al* 2020 Handheld endomicroscope using a fiber-optic harmonograph enables real-time and in vivo confocal imaging of living cell morphology and capillary perfusion *Microsyst. Nanoeng.* **6** 72

[60] Haindl R *et al* 2020 Ultra-high-resolution SD-OCM imaging with a compact polarization-aligned 840 nm broadband combined-SLED source *Biomed. Opt. Express* **11** 3395–406

[61] Yin H, Xiao J and Chen H 2023 CSPA-GAN: a cross-scale pyramid attention GAN for infrared and visible image fusion *IEEE Trans. Instrum. Meas.* **72** 1–11

[62] White R M *et al* 2008 Transparent adult zebrafish as a tool for in vivo transplantation analysis *Cell Steam Cell* **2** 183–9

[63] Guo Z, Li G and Chen S-L 2018 Miniature probe for all-optical double gradient-index lenses photoacoustic microscopy *J. Biophoton.* **11** e201800147

[64] Hajireza P, Shi W and Zemp R 2013 Label-free in vivo GRIN-lens optical resolution photoacoustic micro-endoscopy *Laser Phys. Lett.* **10** 055603

[65] Lin H, Liao C-S, Wang P, Kong N and Cheng J-X 2018 Spectroscopic stimulated Raman scattering imaging of highly dynamic specimens through matrix completion *Light Sci. Appl.* **7** 17179

[66] Deguchi T, Bianchini P, Palazzolo G, Oneto M, Diaspro A and Duocastella M 2020 Volumetric Lissajous confocal microscopy with tunable spatiotemporal resolution *Biomed. Opt. Express* **11** 6293–310

[67] Bondu M, Marques M J, Moselund P M, Lall G, Bradu A and Podoleanu A 2018 Multispectral photoacoustic microscopy and optical coherence tomography using a single supercontinuum source *Photoacoustics* **9** 21–30

[68] Billeh Y N, Liu M and Buma T 2010 Spectroscopic photoacoustic microscopy using a photonic crystal fiber supercontinuum source *Opt. Express* **18** 18519–24

[69] Buma T, Wilkinson B C and Sheehan T C 2015 Near-infrared spectroscopic photoacoustic microscopy using a multi-color fiber laser source *Biomed. Opt. Express* **6** 2819–29

[70] Zhu J, Chen J, Amjadian M, Liang S, Qu Z, Wang Y, Zhang Y and Wang L 2023 Simultaneous dual-modal photoacoustic and harmonic ultrasound microscopy with an optimized acoustic combiner *Biomed. Opt. Express* **14** 1626–35

[71] Park J *et al* 2021 Quadruple ultrasound, photoacoustic, optical coherence, and fluorescence fusion imaging with a transparent ultrasound transducer *Proc. Natl Acad. Sci.* **118** e1920879118